

AperTO - Archivio Istituzionale Open Access dell'Università di Torino

**Lithostratigraphy and petrography of the Monte Banchetta-Punta Rognosa oceanic succession (Troncea and Chisonetto Valleys, western Alps)**

**This is the author's manuscript**

*Original Citation:*

*Availability:*

This version is available <http://hdl.handle.net/2318/1719866> since 2019-12-20T19:03:42Z

*Published version:*

DOI:10.4454/ofioliti.v44i2.526

*Terms of use:*

Open Access

Anyone can freely access the full text of works made available as "Open Access". Works made available under a Creative Commons license can be used according to the terms and conditions of said license. Use of all other works requires consent of the right holder (author or publisher) if not exempted from copyright protection by the applicable law.

(Article begins on next page)



# UNIVERSITÀ DEGLI STUDI DI TORINO

1  
2  
3  
4  
5  
6  
7  
8  
9  
10  
11  
12  
13  
14  
15  
16  
17  
18  
19  
20  
21

***This is an author version of the contribution published on:***

*Questa è la versione dell'autore dell'opera:*

***Corno A., Mosca P., Borghi A. and Gattiglio M. (2019)***

*Lithostrathigraphy And Petrography Of The Monte Banchetta-Punta Rognosa Oceanic  
Succession (Tronca And Chisonetto Valleys, Western Alps)*

*Ofioliti, 44, 83-95*

***The definitive version is available at:***

*La versione definitiva è disponibile alla URL:*

<https://www.ofioliti.it/index.php/ofioliti/issue/view/49>

22 **Lithostratigraphy And Petrography Of The Monte Banchetta-Punta Rognosa Oceanic**  
23 **Succession (Tronca And Chisonetto Valleys, Western Alps)**

24

25 **Corno<sup>1</sup> A., Mosca<sup>2\*</sup> P., Borghi<sup>1</sup> A. and Gattiglio<sup>1</sup> M.**

26

27 *1- Dipartimento di Scienze della Terra, Università degli Studi di Torino, 10125 Torino, Italia*

28 *2- Istituto di Geoscienze e Georisorse, CNR, 10125 Torino, Italia*

29

30 \* Corresponding author: [pietro.mosca@cnr.it](mailto:pietro.mosca@cnr.it)

31

32 **Key word: Ophiolite, metamorphism, mineral chemistry, Western Alps**

33

34 **Abstract**

35 This paper describes lithostratigraphy and Alpine tectono-metamorphic evolution of the oceanic  
36 succession of the Banchetta-Rognosa unit (Italian Western Alps). The oceanic substratum consists  
37 of serpentinised peridotite variably covered at its top by ophicarbonates, documenting therefore  
38 exhumation and exposure of the upper mantle at the seafloor in Jurassic times. Upward, the  
39 sedimentary cover begins with polymictic metabreccia and intercalated siliciclastic sediments  
40 (considered Late Jurassic - Early Cretaceous in age), both containing oceanic and continental  
41 detritus, and interpreted as mass-flow deposits on sea floor. Then, the upper part of the cover  
42 consists of Cretaceous pelagic carbonate sediments (calcschist), lying over a main unconformity.  
43 The stratigraphic features and the architecture of the sedimentary cover suggests that this segment  
44 of the Piemonte-Ligurian ocean was in a proximal position of the rifted margins. In a general  
45 context of the ocean-continent transition, source areas for continental detritus can be envisaged on  
46 the hyperextended part of the European margin or on its more proximal part, resting adjacent to  
47 structural highs made of oceanic mantle as recorded by oceanic detritus. The combination of  
48 structural, petrographic and mineral chemistry data defined the Alpine prograde and retrograde  
49 metamorphic evolution of this oceanic segment. The metamorphic peak was reached during the D1

50 event at the transition between lawsonite- and epidote- blueschist facies conditions. Then, a first  
51 decompressional event D2 always at blueschist facies conditions was followed by a D3 event under  
52 green schist facies conditions.

53

## 54 **Introduction**

55 The Piemonte-Ligurian zone of the Western Alps (as well as of Corsica and Northern Apennines)  
56 includes remnants of the oceanic basin opened during Middle to Late Jurassic between the  
57 European and the Adriatic/African plates (e.g. Lemoine et al., 1986; Lemoine and Trümpy, 1987;  
58 De Wever and Baumgartner, 1995; Froitzheim and Manatschal 1996). This zone consists of  
59 portions of the upper oceanic lithosphere (generally serpentized mantle peridotite, and subordinate  
60 gabbros and pillow basalts) and related Middle Jurassic to Cretaceous pelagic sediments that were  
61 variably involved, dismembered and metamorphosed to HP/UHP conditions in the Alpine nappe  
62 stacking during Tertiary subduction- and collision-related processes. A very abundant literature  
63 distinguished several units (from local to regional scale) in the Piemonte-Ligurian zone of the  
64 Western Alps on the basis of lithostratigraphy and/or Alpine metamorphic evolution (e.g. Elter,  
65 1971; Lagabrielle et al., 1984; Deville et al., 1992; Fudral et al., 1994; Martin et al., 1994; Barfety  
66 et al., 1995; Servizio Geologico di Italia, 2002, and references therein). In this frame, the  
67 stratigraphic features of the sedimentary succession can be used to identify which segment of the  
68 oceanic basin with respect to the rifted continental margins has been sampled and preserved in the  
69 Alpine units.

70 With the purpose to give a contribution to the knowledge of the Piemonte-Ligurian zone and  
71 eventually its relationships with adjacent domains, this paper deals with a poorly investigated  
72 oceanic succession exposed along the Monte Banchetta-Punta Rognosa mountain ridge, extending  
73 between the Troncea and the Chisonetto valleys (Piemonte, NW Italy) in the core of the Western  
74 Alps (Fig. 1). The paper is based on detailed field investigations integrated and supported by  
75 petrological and mineral chemistry analyses. Main scopes are 1) to improve the knowledge of

76 lithostratigraphy of this poorly known and highly deformed succession, and 2) to define the main  
77 steps of its Alpine metamorphic evolution. The chronology of fabrics and structures described in the  
78 following sections has been obtained by the mutual calibration and integration of outcrop  
79 investigations and textural relationships from petrological studies.

80 A further paper will be dedicated to a more detailed description of the structural features (from  
81 outcrop to map scale) of the recognized deformation events, which elements are only simplified in  
82 the map of Fig. 1 due to the purposes of the present paper.

83

84

### 85 **Geological outline**

86 The Piedmont-Ligurian Ocean (part of the western Tethys) opened from the Middle Jurassic  
87 onward between the European and Adriatic/African plates. As a consequence of Europa-Adria  
88 convergence/subduction in Late Cretaceous and continental collision during Tertiary times (e.g.  
89 Tricart, 1984; Roure et al., 1990; Beltrando et al., 2010 and references therein), segments of the  
90 oceanic lithosphere and related sediments were metamorphosed, deformed and stacked with  
91 portions of both the continental margins to form the Alpine Axial Belt (Fig. 1a).

92 Primary relationships of adjacent serpentized mantle and continental units and syn-post-rift  
93 sediments (supported by geochemical studies) have been used to identify the part of the ocean  
94 adjacent to the hyper-extended continental margin (e.g. Dal Piaz, 2010 and references therein),  
95 envisaging then the occurrence of extensional allochthons directly on the exhumed mantle  
96 (Manatschal, 2004; Manatschal and Müntener 2009; Mohn et al., 2012).

97 The typical features of the ophiolitic sedimentary cover are represented by Middle-Upper Jurassic  
98 Mn-rich metachert and marble, and (Upper Jurassic)-Cretaceous calcschists (original marine  
99 calcareous-argillaceous successions), these latter showing variable occurrence of detrital  
100 intercalations from oceanic lithosphere and/or continental margin (e.g. Lemoine 1971; Lagabriele  
101 et al. 1984; De Wever et al., 1987; Lemoine and Tricart, 1986). However, it is important to

102 emphasize that part of the Upper Jurassic-Cretaceous carbonatic metasediments often included in  
103 the oceanic Piemonte-Ligurian zone might be more correctly interpreted as successions deposited in  
104 outer sectors of the oceanic domain in correspondence of the rifted continental margins (Deville et  
105 al., 1992). The Alpine tectono-metamorphic evolution of the ophiolite-bearing successions recorded  
106 generally a subduction-related prograde path with HP blueschist or eclogite-facies metamorphic  
107 peak (and locally UHP), and a subsequent exhumation-related retrograde path (e.g. Beltrando et al.  
108 2010). At the regional scale of the Western Alps, two principal groups of oceanic units are  
109 identified (e.g. Martin et al., 1994; Agard et al., 2002; Angiboust et al., 2009; Dal Piaz 2010 and  
110 references therein). The oceanic eclogitic facies units (or Zermatt-Saas) at lower structural levels,  
111 and the overlying oceanic blueschist facies units (or Combin). In addition, at the highest structural  
112 levels of the oceanic units, the Chenaillet unit forms a klippe of oceanic lithosphere with no post-rift  
113 sediments and escaped from HP-LT subduction-related metamorphism, being only weakly  
114 deformed during its tectonic emplacement in the present nappes stack (Mevel et al., 1978; Bertrand  
115 et al., 1982; Chalot-Prat, 2005).

116 The oceanic sequence discussed in this paper is exposed in a small area (only a few Km<sup>2</sup>) along the  
117 Monte Banchetta-Punta Rognosa ridge (at an altitude between 1800m and 3280ma.s.l.). In this area,  
118 serpentinites and dolostones within continuous sequences of calcschists were already reported in the  
119 earlier Italian geological maps (Servizio Geologico di Italia, 1910). Caron (1971) first mapped and  
120 described the complex juxtaposition between an internal Briançonnais unit (consisting of pre-  
121 Triassic continental basement and a thin and discontinuous Mesozoic cover) and a Piemonte s.l.  
122 unit, made up of dolomitic marbles and dolomitic breccias often associated with serpentinites, and  
123 calcschists. The geological map by Fioraso (2009) well displays the complex geological setting of  
124 this area. In the geological map prepared by the Servizio Geologico di Italia (*in press*), the oceanic  
125 succession here investigated has been included in the composite Monte Banchetta-Punta Rognosa  
126 tectonic unit (Fig. 1c). This unit consists of two parts: an oceanic complex (object of this study) and  
127 a continental complex that are intensively deformed by Alpine metamorphic and post-metamorphic

128 structures. The Monte Banchetta-Punta Rognosa unit dips towards the W at a regional scale, and it  
129 is juxtaposed to several blueschist facies oceanic units bounded by syn- to post-metamorphic  
130 contacts (Fig. 1b). Among these units, the Lago Nero unit rests at an upper structural position and  
131 below the non-metamorphic Chenaillet unit (Polino, 1984). The Lago Nero unit consists of  
132 ophiolites overlain by radiolarian chert (Oxfordian-Kimmeridgian), metalimestone (Late Jurassic-  
133 earliest Cretaceous), argillaceous sands alternating with micritic limestones (Replatte Formation of  
134 Early Cretaceous age) and a sequence of mainly carbonate sediments (calcschist *Auct.*) including  
135 black shales (spanning from Middle to Late Cretaceous). This supra-ophiolite metasedimentary  
136 cover is typically characterized by intercalations of continental and ophiolitic detritus at several  
137 stratigraphic levels (Polino and Lemoine 1984; Burrioni et al., 2003; Servizio Geologico di Italia  
138 2002 and *in press*). The Albergian unit consists of thick sequences of carbonate metasediments with  
139 scattered blocks of ophiolites and related thin sedimentary cover. The Lago Nero and Albergian  
140 units recorded a metamorphic peak in lawsonite-blueschist facies conditions (Servizio Geologico di  
141 Italia, 2002; Malusà et al, 2002). The epidote-blueschist facies Cerogne-Ciantiplagna unit,  
142 juxtaposed to the Banchetta-Rognosa unit by high-angle post-metamorphic faults, consists of a  
143 thick sequence of calcschists embedding very small and isolated blocks of ophiolites (Caron, 1971;  
144 Servizio Geologico di Italia, 2002).

145

## 146 **Lithostratigraphy**

147 Fig.2 is the reconstruction of the oceanic succession of the Monte Banchetta- Punta Rognosa unit as  
148 obtained by correlation and interpretation of several lithostratigraphic logs during field  
149 investigations. This section describes lithostratigraphic features of this succession as observed in the  
150 outcrops.

151 Serpentinite forms outcrops up to 100-m thick. It is both massive and coarse-grained, well  
152 preserving crystals (a few cm in size) of the pyroxene of the original peridotite (Fig. 3a), and  
153 intensively foliated with fibrous serpentine along the foliation planes. In many outcrops,

154 serpentinite has a brecciated texture, from 1 to 5 m thick, towards the overlying sediments, with 1-  
155 50 cm large serpentinite clasts bounded by an irregular network of veins (<1-3 cm thick) filled by  
156 calcite, dolomite and locally talc. This breccia can be referred to as ophicarbonate.

157 The overlying sedimentary succession starts with a polymictic metabreccia, ranging in thickness  
158 from few meters to 30 m, extensively exposed along the western and eastern sides of the Monte  
159 Banchetta (Fig. 1c). However, Caron (1971) has reported also a thin level of (probable) radiolarian  
160 chert directly on the serpentinite. The metabreccia has a block-in-matrix fabric: the matrix is an  
161 impure marble, often containing abundant Fe-oxides. The clasts, wrapped by the pervasive foliation  
162 and locally up to a few meters in size, consist of serpentinite, ophicarbonate (Fig. 3b), and  
163 subordinate gneiss, micaschist (Fig. 3c) and dolomitic marble. At the western side of the Monte  
164 Banchetta, a block of metagabbro with a well-preserved magmatic texture has been found (Fig. 3d).  
165 In the south-eastern sector of the Monte Banchetta, the polymictic metabreccia displays a decrease  
166 of clast size from the underlying serpentinite, and progressively passes upward into a fine-grained  
167 impure marble (showing a maximum thickness of ~10 m), defining then a broad fining upward  
168 sequence.

169 Bodies of white-greenish metasandstone (Figs. 3e, 3f and 3g), with maximum thickness of ~15 m  
170 and 50-60 m long, have been variably observed with pinch-out terminations both intercalated and  
171 on the top of the polymictic metabreccia. Similar sediments have been locally observed also directly  
172 on serpentinites and ophicarbonates. The metasandstone is often characterized by the widespread  
173 occurrence of Fe-oxides aggregates (up to cm in size) and large white micas and chlorite flakes  
174 along the pervasive foliation planes. Locally, discontinuous micro-conglomerate (<50 cm thick)  
175 with mm to cm clasts of quartz and levels of white to gray impure quartzite have been observed  
176 associated with the metasandstone. The metasandstone has a few intercalations of green to bluish  
177 horizons (<50 cm thick) of mafic composition, rich in glaucophane and chlorite (Fig. 3f). The  
178 metasandstone is capped by calcschist (described below) in its uppermost part, and it contains clasts

179 and rare blocks up to a few meters in size of dolomitic marble and dolomitic metabreccia elongated  
180 between the foliation planes (Fig. 3g and Fig. 1c).

181 The uppermost part of the sedimentary succession consists of calcschist, at least 100-200m thick  
182 and unconformably overlaying serpentinite-ophicarbonates and related sediments (Figs. 1c and 3e).

183 In the calcschist, primary compositional features are suggested by alternating cm to dm thick  
184 carbonate- and silica-rich domains, by discontinuous intercalations of impure marble, black and  
185 dark green schist (10 cm to 2 m thick). In addition, scattered blocks of serpentinite, metabasite and  
186 dolomitic metabreccia are embedded in the calcschist, generally stretched between the foliation  
187 planes.

188

### 189 **Structural setting**

190 Four main deformation events (D1-D4) can be identified in the oceanic succession. Petrographic  
191 description of the different planar fabrics related to these events are detailed in the following  
192 section. The oldest event D1 is recorded by the foliation S1, preserved in microlithons, intrafolial  
193 folds and isolated fold hinges. S1 results sub-parallel to primary compositional banding/ lithological  
194 contacts (Fig. 3d) and is defined by Na-pyroxene + serpentine ± magnetite ± amphibole in  
195 ultrabasic rocks, Na-pyroxene + Na-amphibole ± quartz in basic rocks and quartz + phengite + Na-  
196 amphibole + chloritoid in pelitic rocks. S1 foliation (together with lithological contacts) is deformed  
197 and transposed during D2 into tight to isoclinal folds (Fig. 3f). The axial plane schistosity S2 is  
198 usually the most penetrative planar fabrics in the outcrops. S2 is mainly defined by aegerin-augite +  
199 serpentine + amphibole in ultrabasic rocks, aegerin-augite + phengite + epidote in basic rocks and  
200 quartz + phengite + garnet ± chloritoid + chlorite in pelitic rocks. A L2 stretching lineation is  
201 marked by alignment of phengite, amphibole, chloritoid or locally tourmaline on the S2. Kinematic  
202 indicators and relationships between L2 on S2 and fold geometries suggest an E- to SE verging non-  
203 cylindrical folding during D2 (Fig. 3h). D3 is recorded by folds and crenulations with ENE-WSW  
204 trending sub-horizontal axes and axial planes usually dipping at high angle to SSE (Fig. 3f).

205 Chlorite + tremolite + muscovite + stilpnomelane assemblage defines a locally pervasive S3. A late  
206 D4 led to the development of gentle kilometer-scale folds with N-S trending axes and with axial  
207 planes dipping at high angle.

208

### 209 **Petrology and mineral chemistry**

210 This section deals with main textural relationships and mineral chemistry of rocks forming the  
211 oceanic succession. –. A Scanning Electron Microscope (JEOL JSM-IT300LV) equipped with an  
212 energy-dispersive X-ray spectrometer (EDX), with a SDD (a silicon drift detector from Oxford  
213 Instruments), hosted at the Earth Science Department of the University of Turin, was used for the  
214 determination of major elements. The experimental conditions include: accelerating voltage 15 kV,  
215 counting time 50 s, process time 5  $\mu$ s and working distance 10mm. The measurements were  
216 conducted in high vacuum conditions. The EDX acquired spectra were corrected and calibrated  
217 both in energy and in intensity thanks to measurements performed on cobalt standard introduced in  
218 the vacuum chamber with the samples. The Microanalysis Suite Oxford INCA Energy 300, that  
219 enables spectra visualization and elements recognition, was employed. A ZAF data reduction  
220 program was used for spectra quantification. The resulting full quantitative analysis is obtained  
221 from the spectra, using natural oxides and silicates from Astimex Scientific Limited\_ as standards.  
222 All the analyses were recalculated using the MINSORT computer program (Petraakis and  
223 Dietrich, 1985). Representative selection of mineral composition is reported in Table 1 of the  
224 supplementary material. Fig. 4 and Fig. 5 show representative microstructures and Fig. 6 reports  
225 chemical composition and classification diagrams of representative minerals. Fig. 7 summarizes the  
226 parageneses developed during the different deformation stages.

227

### 228 *Serpentinite*

229 The serpentinite consists of serpentine + pyroxene + amphibole + chlorite  $\pm$  magnetite  $\pm$  carbonate  
230 with variable occurrence of pyrite, calcopyrite, ilmenite and titanite. Coarse grained serpentinite

231 preserves crystals (up to a few cm in size) of diopside ( $\text{Na} < 10 \text{ wt\%}$  and  $\text{XMg} > 0.9$ , showing very  
232 low content in Cr ranging between 0.4 and 0.7 wt%) and magnetite of the original peridotite (Figs.  
233 4a and 6a). S1/S2 foliations are defined by serpentine and aegirine-augite, grown after magmatic  
234 pyroxene and in turn replaced by tremolitic amphibole and chlorite weakly isoriented (Fig. 4b). The  
235 associated ophicarbonates show large magnetite and serpentinite fragments separated by different  
236 sets of carbonate-bearing veins (Fig. 4c).

237

### 238 *Polymictic metabreccia*

239 The matrix of the metabreccia (Fig. 4d) is an impure marble consisting of calcite + quartz + Fe-  
240 chlorite + glaucophane + tremolite. S1/S2 foliation is defined by isoriented glaucophane within a  
241 calcite matrix. Fe-chlorite ( $\text{Cr}_2\text{O}_3 \sim 3 \text{ wt\%}$  and  $\text{MnO} \sim 1.57 \text{ wt\%}$ ) and tremolite (Amph D3, Fig. 6b)  
242 mark the S3 foliation.

243 The clast of metagabbro preserves evidences of an original coarse-grained magmatic texture (Figs.  
244 3d, 4e and 4f). Large aggregates, up to few cm in size, of epidote + white mica + albite replaced  
245 magmatic plagioclase. They are dispersed within a fine-grained assemblage of Na-Ca pyroxene +  
246 Mg-chlorite + epidote replacing original magmatic pyroxenes. The Na-Ca pyroxene displays  
247 omphacitic core (recording D1 event) and aegirine-augite rim (D2 event), and have acmitic content  
248 up to 30% (Fig. 4f and Fig. 6a). The S2 foliation is defined by Na-Ca pyroxene + phengite  
249 ( $\text{Si} \sim 3.30\text{-}3.40 \text{ a.p.f.u.}$ , Fig. 6d). The later S3 foliation is marked by Mg-chlorite + muscovite (after  
250 phengite,  $\text{Si} < 3.30 \text{ a.p.f.u.}$ , Fig. 6d) + zoisite (with contents  $< 1\%$  of  $\text{Cr}_2\text{O}_3$  e  $\text{MnO}$ )  $\pm$  allanite (epidote  
251 rich in Ce, La and Nd). Late pumpellyite crystals are also present. The clasts of gneiss (stretched  
252 along the S2) contains assemblage of chlorite + muscovite + opaque after pyroxene enveloped by a  
253 foliation defined by chlorite + albite + fine-grained sericite (Fig. 4g).

254

### 255 *Metasandstone*

256 The metasandstone consists of quartz (ranging from 70-90% in volume of total rock) + white mica  
257 + Fe-chlorite + chloritoid + glaucophane with variable amounts of stilpnomelane, tourmaline,  
258 calcite, apatite and rutile. This rock usually displays a lepidoblastic texture with the pervasive S2  
259 foliation defined by quartz + chloritoid + white mica (generally zoned, with phengite at the core and  
260 muscovite at the rim, Fig. 6d), transposing an earlier S1 foliation of quartz + phengite +  
261 glaucophane + chloritoid + rutile. The late S3 foliation is marked by isoriented Fe-chlorite +  
262 muscovite + stilpnomelane. A primary micro-conglomeratic fabric is recorded by elongated and  
263 sub-rounded quartz grains wrapped by the S2 foliation. The white to gray impure quartzite shows  
264 fine-grained assemblages of quartz (more than 90% of the total rock) ± white mica ± calcite.

265 The mafic horizons intercalated in the metasandstone (Fig. 4h) consist of abundant glaucophane  
266 (Fig. 6b), white mica and quartz with minor and variable amount of calcite, pyrite, zircon, apatite  
267 and detrital allanite. In these horizons, nematoblasts of medium-grained glaucophane + phengite (Si  
268 < 3.50, Fig. 6d) + quartz define the S2 foliation, while assemblage of quartz + glaucophane +  
269 phengite (Si > 3.50, up to 3.72 a.p.f.u., Fig. 6d) rutile marks a S1 foliation in microlithons. A locally  
270 very pervasive S3 crenulation cleavage is defined by muscovite + chlorite + albite (An < 5%) +  
271 quartz.

272

### 273 *Calcschist*

274 The calcschist consists of carbonate, ± quartz, white mica, chlorite and graphite, with minor  
275 tourmaline and apatite. Monocrystalline quartz is irregularly distributed within the carbonate  
276 matrix, ranging from 10% to 30% of the rock. White mica is oriented along S1 and the main S2  
277 foliation. Aggregates containing white mica + graphite ± zoisite relics within the S1 foliation can be  
278 interpreted as pseudomorphs after lawsonite (Fig. 5a). Calcite + white mica + quartz define S2  
279 foliation.

280 Pyroxene-bearing metabasite (Fig. 5b) embedded in the calcschist consists of Na-amphibole +  
281 tremolite + chlorite + epidote + titanite + pumpellyite ± albite. It shows a nematoblastic texture with

282 pyroxene of aegirine-augite (Fig. 6a) composition partially replaced by glaucophane (Amphibole  
283 D2 in Fig. 6b), that with epidote, white mica, chlorite and titanite defines the S2 foliation.  
284 Amphibole of tremolitic composition (Amphibole D3 in Fig. 6b) has been observed in paragenesis  
285 with green chlorite and Cr-rich pumpellyite ( $\text{Cr}_2\text{O}_3$  content is ~4.5-5.5 wt%) to define S3.  
286 The intercalations of black schist (Figs. 5c and 5d) are mainly composed of quartz + garnet +  
287 stilpnomelane + chlorite + calcite + pyrite and have high contents of ankerite and Fe-Mn oxides.  
288 Usually, in this rock the S2 foliation is marked by white mica and chlorite films.  
289 Garnet subhedral to euhedral porphyroblasts are syn-kinematic with respect to S2 and include an  
290 earlier S1 foliation consisting of white mica + quartz + graphite. This garnet is usually Mn-rich  
291 (Fig. 6c) with spessartinic end-member up to 40-50%, and has a Mg content < 0.30 wt% (see Table  
292 1, supplementary material). Grossular content is usually around 15% while almandine can reach  
293 40%. Although a compositional cross-section has been carried out, no chemical zoning has been  
294 identified. The anomalous enrichment in Mn can be due to the original chemical composition of the  
295 protolith. Often, largest crystals of garnet are rimmed by late Mn-rich ankerite (Fig. 5c).  
296 Stilpnomelane (from yellowish bronze to dark brown in colour) grows both after garnet and in  
297 fractures (Fig. 5d).  
298 The dark green schist, forming discontinuous levels in the calcschist, consists of white mica +  
299 stilpnomelane + chlorite + quartz + calcite/dolomite with variable quantities of Fe-Mn ankerite,  
300 ilmenite and titanite. Relics of the S1 foliation are defined by amphibole (in turn replaced by  
301 chlorite) and white mica. White mica is typically zoned showing phengitic core with high content  
302 (up to 3.75 a.p.f.u., Fig. 6d) and has a content of  $\text{Cr}_2\text{O}_3$  of ~ 3 wt%. White mica-rich layers are often  
303 strongly crenulated with development of S3 axial plane foliation defined by chlorite and  
304 stilpnomelane.

305

## 306 **Metamorphic evolution**

307 Metamorphic conditions of the oceanic succession have been reconstructed by combining  
308 microstructural observations, chemical analyses and conventional P-T thermobarometric estimates  
309 (Fig. 8).

310 The recognition of pseudomorphs after lawsonite, observed as structural relic within the calcschist,  
311 constrains the burial path in the stability field of lawsonite bearing blueschist facies, characterized  
312 by low metamorphic gradient (Chen et al., 2013).

313 During the first tectono-metamorphic event D1, the metamorphic peak is defined by the omphacite  
314 + zoisite + glaucophane + rutile paragenesis developed in the basic system.

315 The occurrence of Na-amphibole in the metabasites implies P conditions lower than those of the  
316 amphibole vs chloritoid transition (Poli and Schmidt, 1995). Evidences of the HP metamorphism  
317 are also represented by the occurrence of the chloritoid + glaucophane assemblage in the  
318 metasandstone.

319 The maximum extension of the stability field of the chloritoid-glaucophane association, calculated  
320 for the NKFMAASH system (Proyer, 2003), partly overlaps with the lawsonite blueschist facies and  
321 is indicative of temperatures between 420 ° C and 600 ° C and pressures of ~1.9 GPa. The aforesaid  
322 stability field, however, can sensibly expand as a function of the increase of Fe<sup>3+</sup> in these two  
323 minerals, up to partially overlap with the field of the epidote blueschist facies (Guiraud et al., 1990).

324 The results of the analyses indicated a XFe<sup>3+</sup> content ranging from 0.1 to 0.2 in chloritoid and 0.4 -  
325 0.5 for amphibole, and then a range of P-T conditions near the transition between the lawsonite -  
326 epidote blueschist facies can be inferred (Fig. 8). The P-T peak conditions can therefore be  
327 estimated at approximately 470-520 ° C, at 1.7-1.9 GPa. These conditions are in agreement with the  
328 high Si content of phengite occurring in the mafic horizons in the metasandstone (Si ≈3.50-3.75  
329 a.p.f.u., Fig. 6d) and in the levels of dark green schist within calcschist (Si ≈3.60- 3.75 a.p.f.u., Fig.  
330 6d), that, according to phengite geobarometry of Massonne and Schreyer (1987), implies minimum  
331 P values of 1.7 - 1.9 GPa for T of around 500°C.

332 The second metamorphic stage (D2) is generally identifiable as the main tectonic-metamorphic  
333 event. The mineral assemblage (epidote, aegirine-augite, Na-Ca-amphibole and chlorite in  
334 metabasite) indicates that, according to Palin and White (2016), this second metamorphic stage  
335 developed under epidote-blueschist to epidote-amphibolite-facies transition. The occurrence of  
336 chlorite in the basic system points out that the upper limit of chlorite + quartz stability field  
337 calculated by Poli and Schmidt (1995) was not exceeded. These conditions are in agreement with  
338 the Si content ( $\leq 3.40$  a.p.f.u of phengite growth in the metagabbro and in the metasandstone (Fig.  
339 6d), that, according to phengite geobarometry of Massonne and Schreyer (1987), implies minimum  
340 P values of 0.9-1.1 GPa for T around 500°C. In addition, syn-cinematic D2 garnet (characterized by  
341 high Mn content) suggests that the temperature reached during its growth has never exceeded 500 °  
342 C (Spear and Cheney, 1989).

343 The subsequent D3 event is characterized by typical parageneses of the greenschist facies  
344 conditions. In the metagabbro, zoisite is replaced by clinozoisite and Ca-amphibole. Chlorite and  
345 albite pervasively grew after omphacite. In metabasite, Na-amphibole is replaced by Ca-amphibole  
346 (Fig. 6b) and albite, whereas garnet and rutile are replaced by chlorite and titanite, respectively. The  
347 white mica related to D3 event is characterized by a low Si content ( $< 3.30$  a.p.f.u., Fig. 6d). The  
348 stilpnomelane + chlorite assemblage in metasandstone and black and dark green schists implies  
349 temperature lower than 400 °C.

350

### 351 **Remarks and conclusion**

352 Data discussed in this paper allow i) to propose a detailed model for the depositional history of the  
353 oceanic segment of the Monte Banchetta-Punta Rognosa unit and ii) to trace its Alpine tectono-  
354 metamorphic evolution.

355 The presence of serpentinised peridotite covered at their top by ophicarbonates generally records  
356 exhumation and exposure of the upper mantle at the seafloor in Jurassic times. Then, after  
357 discontinuous deposition of Middle-Upper Jurassic radiolarian chert (Caron 1971), the exposed

358 mantle has been directly covered by the polymictic breccia (metabreccia) and intercalated  
359 siliciclastic sediments (metasandstone), both representing mass-flow deposits on sea floor and  
360 characterized by oceanic and continental clasts and blocks. The upper part of the sedimentary cover  
361 records the unconformable deposition of pelagic carbonate-rich sediments (calcschist), poor of  
362 oceanic and continental detritus. The largely accepted Cretaceous age for the calcschist deposition  
363 suggests to refer the underlying polymictic breccia and intercalated sandstones to the Late Jurassic -  
364 Early Cretaceous.

365 The polymictic breccia and intercalated sandstones indicate the close presence of structural highs  
366 made of oceanic and continental rocks in response to the Jurassic rifting (e.g. Beltrando et al.,  
367 2014). Source areas for serpentinite, ophicarbonates and gabbro clasts (mainly prevailing in the  
368 lowermost stratigraphic parts) can be envisaged on a paleo-topography of exhumed mantle,  
369 probably controlled by extensional faults. The continental detritus in the polymictic breccia,  
370 represented by platform deposits (dolostone and dolomitic breccia) usually considered Triassic (-  
371 Early Jurassic?) in age (e.g. Dal Piaz, 2010 and therein references) and pre-Triassic rocks (gneiss  
372 and micaschist), suggests that this oceanic segment was in a proximal position to the rifted  
373 European margin. In a general context of the ocean-continent transition, continental source areas  
374 can be envisaged on the hyperextended part of the European margin or on its more proximal part.  
375 The observed enrichment in Mn and Cr contents and widespread occurrence of Fe-oxides in these  
376 mass-flow deposits document presence of exposed mantle.

377 Close association of continental and oceanic detritus in the supra-ophiolite sedimentary cover were  
378 described in several oceanic sections in these regions of the Western Alps (e.g. Caby et al., 1971;  
379 Lagabrielle, 1981; Lagabrielle et al., 1984; Polino and Lemoine, 1984; Balestro et al., 2015 e  
380 Tartarotti et al 2017). In the investigated region, mixed detritus typically characterizes the Jurassic-  
381 Cretaceous sediments of the Lago Nero unit (Polino and Lemoine, 1984; Servizio Geologico di  
382 Italia, 2002 and *in press*), resting to the west of Monte Banchetta-Punta Rognosa unit in an upper  
383 structural position (Fig. 1b). On the basis of this stratigraphic feature, a proximal position with

384 respect to the European margin has been usually proposed in literature for this unit. Therefore,  
385 according to this interpretation, the oceanic segments of the Lago Nero and Monte Banchetta- Punta  
386 Rognosa units could be tentatively restored in a similar place.

387 However, Burrioni et al. (2003) suggested that Upper Cretaceous calcschists (Gondran flysch) of the  
388 Lago Nero unit are covered by mass-gravity deposits (the Rocher Renard complex made up of dark  
389 schist with oceanic blocks). Due to this setting, Burrioni et al. (2003) proposed that the upper mass-  
390 gravity deposits derived from erosion of the accretionary wedge during converging processes and  
391 then, in an alternative view, placed the Lago Nero oceanic segment in an internal position of the  
392 Piemonte-Ligurian realm. Therefore, taking into account this alternative interpretation, the Lago  
393 Nero unit and the Monte Banchetta-Punta Rognosa unit would identify two different oceanic  
394 segments, in internal and external (pericontinental) position respectively.

395 Petrological and mineralo-chemical analyses constrain a metamorphic peak (D1) at the transition  
396 between lawsonite- and epidote- blueschist facies conditions, followed by a first decompressional  
397 event (D2) always inside the blueschist facies conditions for the oceanic succession of the Monte  
398 Banchetta-Punta Rognosa unit. Then a third event (D3) under green schist facies conditions  
399 occurred. Considering the limited reduction of temperature identified by the transition from D1 to  
400 D2, the trajectory of exhumation of the investigated succession seems to be characterized by a  
401 rather rapid exhumation.

402 As a general conclusion, this paper documented primary stratigraphic relationships, related and  
403 following the Jurassic rifting, in a poorly known unit highly deformed by tectono-metamorphic  
404 events. However, data presented must be considered as a starting point for further multidisciplinary  
405 studies, aimed in particular to give constraints to the Jurassic paleogeographic scenario of this sector  
406 of the Alps, still variously debated and interpreted in literature.

407

408 **Acknowledgements**

409 We are very grateful to Gianreto Manatschal, Luca Barale and Nicolò Incerpi for the discussion on  
410 the topics of present paper during a field excursion. Gisella Rebay and anonymous reviewer are  
411 acknowledged for their constructive comments, and remarks, which improved the manuscript.

412

## 413 Captions

414

415 **Figure 1: Geological setting.** a) tectonic sketch map of the Western Alps. Inset shows location of  
416 Fig. 1b (simplified after Molli et al., 2010); b) tectonic sketch of the investigated region (redrawn  
417 after Servizio Geologico di Italia, *in press*); c) Simplified interpretative geological map of the  
418 Monte Banchetta-Punta Rognosa area based on the results of this study (only regional attitude of the  
419 S2 foliation and main tectonic contacts are reported; see text for details).

420

421 **Figure 2: Lithostratigraphy of the oceanic succession.**

422

423 **Figure 3: Representative lithologies at the mesoscale.** a) detail of massive serpentinite with  
424 magmatic pyroxene relics (Px) (sample AC82); b) serpentinite clasts ( $\Sigma$ ) in the lower part of the  
425 polymictic metabreccia (Monte Banchetta south-eastern side, 1940m); c) continental clast (mcs:  
426 micaschist) in the polymictic metabreccia (Monte Banchetta summit, 2823m); d) metagabbro block  
427 in the polymictic metabreccias (Monte Banchetta western side, 2573m); e) metasandstone (ms)  
428 intercalated in the polymictic metabreccia (br) between Passo della Banchetta and Monte Banchetta  
429 summit (cs, calcschist;  $\Sigma$ , serpentinite); f) bluish horizons of mafic composition (mh) in the  
430 metasandstone (ms), deformed by D2 folding and D3 crenulation (PaxF: axial plane; north of La  
431 Grangia, 2040m); g) upper part of the metasandstone containing dolomitic clasts (dol) (south-east of  
432 Passo della Banchetta, 2710m); h) non-cylindrical D2 fold in calcschist (Lest2, stretching lineation;  
433 F2, fold axis) (Monte Banchetta north-west side, 2570m).

434

435 **Figure 4: Representative microstructures.** a) massive serpentinite consisting of serpentine (Srp)  
436 and large pyroxene relics (Di, diopside) (sample AC82); b) aegerine-augite pyroxene grown after  
437 magmatic diopside and replaced by tremolite and chlorite in the serpentinite (sample AC82); c)

438 ophicarbonates made of serpentine (Srp) and magnetite relics (Mag), with multiple sets of carbonate  
439 veins (Cb) (sample AC67); d) carbonatic matrix (cc) of the polymictic metabreccia with Na-  
440 amphiboles (Amp) isoriented to define S2 foliation and partially replaced by chlorite (Chl). Note  
441 widespread occurrence of Fe-oxides (Ox Fe) (sample AC2); e) meta-gabbro with muscovite (Ms) +  
442 epidote (Ep) + albite (Ab) pseudomorphosis after plagioclase and fine-grained matrix made of  
443 omphacite (Omp) + chlorite (Chl) ± epidote (Ep) replacing magmatic pyroxene (sample AC12); f)  
444 Na-Ca pyroxene with omphacitic (Omp) core and aegirine-augite (Aeg) rim, in the metagabbro  
445 (sample AC 12). Chl, chlorite; g) Clasts of gneiss in the polymictic metabreccia characterized by  
446 aggregates of chlorite (Chl) + muscovite (Mus) + opaque (Opq) after pyroxene (Px); h) mafic  
447 horizons within the metasandstone, showing a foliation defined by glaucophane (Amp) + phengite  
448 (Phe) + quartz (Qz). Note chlorite (Chl) replacing Amp, and isolated Apatite (Ap) grains (SEM  
449 image; sample AC57).

450

451 **Figure 5: Representative microstructures.** a) Pseudomorphs after lawsonite defined by white  
452 mica (Wm) + Quartz (Qz) + graphite (Graph) ± zoisite (Ep) relics of the S1 foliation; b) Pyroxene-  
453 bearing metabasite embedded in the calcschist showing pyroxene of aegirine-augite composition  
454 partially replaced by Na- amphibole. c) spessartinic garnet (Grt) in the black schist; garnet is  
455 rimmed by ankerite rims (Ank) and wrapped by stilpnomelane (Stp) and quartz (Qz) (SEM image;  
456 sample AC15); d) spessartinic garnet (Grt) related to D2 event in the black schist preserves an  
457 internal S1 foliation defined by quartz and white mica (sample AC15). Late stilpnomelane is  
458 statically growing.

459

460 **Figure 6: Chemical composition and classification diagrams.** a) Morimoto (1988) pyroxene  
461 diagram A: Ca-Mg-Fe pyroxenes, B: Na-Ca pyroxenes, C: Na pyroxenes. En: enstatite, Wo:  
462 wollastonite, Fs: ferrosilite, Di: diopside, Hd: hedembergite, Jd: jadeite, Ae: aegirine-augite. b)  
463 Amphibole composition in the Hawthorne et al. (2012) diagram Na vs Al<sup>IV</sup>. c) Garnet composition

464 in almandine (Alm) – spessartine (Sps) – grossular (Grs) diagram. d) White mica composition in the  
465 Si vs  $Al^{IV}+Al^{VI}$  diagram.

466 Note that the shifting shown in figure 6d by the analysis of white mica from different samples is due  
467 to the different content of iron present in the micas (see table 1). In particular, the micas of mafic  
468 horizon are characterized by a lower iron content, while metagabbros and green schists show higher  
469 iron values. In these last micas a a greater amount of trivalent iron replaced the octahedral  
470 aluminium, while in the micas of mafic horizon this substitution is found to be smaller

471

472

473 **Figure 7: mineral assemblage developed during the different deformation stages**

474

475 **Figure 8: Petrogenetic grid.** The green dashed line shows average P-T conditions for the  
476 lawsonite-epidote blueschist peak (D1), blueschist facies (D2) and greenschist facies (D3)  
477 metamorphic events, respectively. The garnet, chlorite, epidote and lawsonite stability curves (5, 6,  
478 8, 10, 12) were taken from Poli and Schmidt (1995), the chloritoid-glaucophane stability fields  
479 from Guiraud et al., 1990, and Proyer, 2003. Other curves: 1) isopleths of  $Si^{4+}$  content in phengite  
480 (Massonne and Schreyer, 1987); 2) transition of blueschist/greenschist facies (Maruyama et al.,  
481 1986); 3) Guiraud et al., 1990; 4) Holland, 1983; 7) Ernst, 1979; 9) Evans, 1990; 11) Corona et al.,  
482 2013.

483 Table 1. Representative SEM-EDX analyses of clinopyroxene (omph = omphacite; aeg-au =  
484 aegirine – augite; diop = diopside) calculated on the basis of 6 oxygens and 4 cations. bdl: below  
485 detection limit.

486 Table 2. Representative SEM-EDX analyses of garnet calculated on the basis of 12 oxygens and 8  
487 cations. bdl: below detection limit. End member abbreviations: alm = almandine; sps = spessartine;  
488 pyr = pyrope; grs = grossular; anr = andradite.

489 Table 3. Representative SEM-EDX analyses of dioctahedral mica calculated on the basis of 11  
490 oxygens and 7 cations. bdl: below detection limit.

491 Table 4. Representative SEM-EDX analyses of amphibole calculated on the basis of 23 oxygens .  
492 bdl: below detection limit.

493 Table 5. Representative SEM-EDX analyses of chloritoid calculated on the basis of 12 oxygens.

494

495

496 **References**

497

498 Agard P., Monie P., Jolivet L. and Goffé B., 2002. Exhumation of the Schistes Lustrés complex: *in*  
499 *situ* laser probe  $^{40}\text{Ar}/^{39}\text{Ar}$  constraints and implications for the Western Alps. *Journal of*  
500 *Metamorphic Geology*, 20, 599-618.

501 Angiboust S., Agard P., Jolivet L. and Beyssac O., 2009. The Zermatt-Saas ophiolite: the largest  
502 (60-km wide) and deepest (c. 70-80km) continuous slice of oceanic lithosphere detached from a  
503 subduction zone? *Terra Nova*, 21, 171-180

504 Balestro G., Festa A. and Tartarotti, P., 2015. Tectonic significance of different block-in-matrix  
505 structures in exhumed convergent plate margins: Examples from oceanic and continental HP rocks  
506 in inner western Alps (northwest Italy). *International Geology Review*, 57: 581–605.

507 Barféty J. C., Lemoine M., de Graciansky P. C., Tricart P. and Mercier D., 1995. Notice explicative  
508 de la feuille Briançon à 1/50 000 (823). Orleans: Ed. du BRGM, Serv. Geol. Nat., 180 p.

509 Beltrando M., Compagnoni R. and Lombardo B., 2010. (Ultra-) High-pressure metamorphism and  
510 orogenesis: An Alpine perspective. *Gondw. Res.*, 18 (1): 147-166.

511 Beltrando M., Manatschal G., Mohn G., Dal Piaz G.V., Vitale Brovarone A. and Masini E., 2014.  
512 Recognizing remnants of magma-poor rifted margins in high-pressure orogenic belts: The  
513 Alpine case study. *Earth-Science Reviews*, 131: 88–115.

514 Bertrand J., Courtin B. and Vuagnat M., 1982. Elaboration d'un secteur de lithosphère océanique  
515 Liguro-Piemontais d'après l'ophiolite de Mongenèvre (Hautes-Alpes, France et province de  
516 Turin, Italie). *Ofioliti*, 2/3: 155-196.

517 Burroni A., Levi N., Marroni M. and Pandolfi L., 2003. Lithostratigraphy and structure of the Lago  
518 Nero Unit (Chenaillet Massif, Western Alps): comparison with internal Liguride units of  
519 Northern Apennines. *Ofioliti*, 28 (1): 1-11

- 520 Caby R., Michard A. and Tricart, P., 1971. Decouverte d'une brèche polygenique à elements  
521 granitoïdes dans les ophiolites metamorphiques piemontaises (Schistes Lustrés du Queyras,  
522 Alpes françaises). C.R. Acad. Sc. Paris, 273: 999–1002.
- 523 Caron J. M., 1971. Contribution a l'étude lithostratigraphique et structurale de la région de Sestrière  
524 (Alpes Cottiennes, Italie). Trav. Lab. Géol. Grenoble, 21, 45-68.
- 525 Chalot-Prat F., 2005. An undeformed ophiolite in the Alps: field and geochemical evidences for a  
526 link between volcanism and shallow plate tectonic processes. In: Foulger G.R., Natland J.H.,  
527 Presnall D.C. and Anderson D.L. (Eds). Plates Plumes & Paradigms, Geological Society of  
528 America, Special Paper 388, p. 751-780.
- 529 Chen Y., Ye K., Wu T. F. and Guo S., 2013. Exhumation of oceanic eclogites: thermodynamic  
530 constraints on pressure, temperature, bulk composition and density. *Journal of Metamorphic*  
531 *Geology*, 31(5): 549-570.
- 532 Corona J.C., Jenkins D.M. and Holland T.J.B., 2013. Constraints on the upper pressure stability of  
533 blueschist facies metamorphism along the reaction: glaucophane = talc + 2 jadeite in the Na<sub>2</sub>O-  
534 MgO-Al<sub>2</sub>O<sub>3</sub>-SiO<sub>2</sub>-H<sub>2</sub>O system. *Am. J. Science*, 313, 967-995.
- 535 Dal Piaz G. V., 2010. The Italian Alps: a journey across two centuries of Alpine geology. In: (Eds.)  
536 Marco Beltrando, Angelo Peccerillo, Massimo Mattei, Sandro Conticelli, and Carlo Doglioni,  
537 *Journal of the Virtual Explorer*, volume 36, paper 8, doi: 10.3809/jvirtex.2010.00234
- 538 De Wever P. and Baumgartner P.O., 1995. Radiolarians from the base of the Supra-ophiolitic  
539 Schistes Lustrés formation in the Alps (Saint-Véran, France and Traversiera Massif, Italy). In:  
540 Baumgartner P.O., O' Dogerthy L, Gorican S, Urquhart E, Pillevuit A, De Wever P (eds) *Middle*  
541 *Jurassic to Lower Cretaceous Radiolaria of Tethys: occurrences, systematics, biochronology.*  
542 *Mém. Geol (Lausanne)* 23:725-730.
- 543 De Wever P., Baumgartner P.O. and Polino R., 1987. Précision sur les datations de la base des  
544 Schistes lustrés post-ophiolitiques dans les Alpes cottiennes. C.R. Acad. Sci., 305(2): 487-491.

- 545 Deville, E., Fudral, S., Lagabrielle, Y., Marthaler, M. and Sartori, M., 1992. From oceanic closure  
546 to continental collision: A synthesis of the " Schistes lustrés" metamorphic complex of the  
547 Western Alps. *Geol. Soc. of Am. Bul.*, 104(2): 127-139.
- 548 Elter G., 1971. Schistes Lustrés et ophiolites de la zone piémontaise entre Orco et Doire Baltée  
549 (Alpes Graies). Hypothèses sur l'origine des ophiolites. *Géol. Alpine (Grenoble)*, 47: 147-169.
- 550 Ernst W. G. 1979. Coexisting sodic and calcic amphiboles from high-pressure metamorphic belts  
551 and the stability of barroisitic amphibole. *Miner. Magazine*, 43(326): 269-278.
- 552 Evans B.W. 1990. Phase relations of epidote-blueschists. *Lithos*, 25: 3-23.
- 553 Fioraso G., 2009. - Carta Geologica della Val Tronca. CNR - Istituto di Geoscienze e  
554 Georisorse, Ente di Gestione Parco Val Tronca, Regione Piemonte. LitografiaGeda –  
555 Nichelino.
- 556 Froitzheim, N. and Manatschal, G., 1996. Kinematics of Jurassic rifting, mantle exhumation, and  
557 passive-margin formation in the Austroalpine and Penninic nappes (eastern Switzerland). *Geol.*  
558 *Soc. of Am. Bul.*, 108(9): 1120-1133.
- 559 Fudral S., Deville E., Pognante U., Gay M., Fregolent G., Lorenzoni S., Robert D., Nicoud G.,  
560 Blake C., Jayko A., Jaillard E., Bertrand J.M., Forno M.G. and Massazza G., 1994. Carte  
561 Géologique de la France à 1:50.000, feuille 776 Lanslebourg - Mont d'Ambin.
- 562 Guiraud M., Holland T. and Powell R. 1990. Calculated mineral equilibria in the greenschist-  
563 blueschist-eclogite facies in Na<sub>2</sub>O – FeO – MgO – Al<sub>2</sub>O<sub>3</sub> – SiO<sub>2</sub> – H<sub>2</sub>O. *Contrib. Mineral.*  
564 *Petrol.*, 104: 85-89.
- 565 Hawthorne F.C., Oberti R., Harlow G. E., Maresch W. V., Martin R.F., Schumacher J. C. and  
566 Welch D., 2012. Nomenclature of the amphibole supergroup. *Amer. Mineral.*, 97: 2031-2048.
- 567 Holland T. J. B., 1983. The experimental determination of activities in disordered and short-range  
568 ordered jadeitic pyroxenes. *Contrib. Mineral. Petrol.*, 82(2-3): 214-220.

569 Lagabrielle Y., 1981. Les schistes lustrés à ophiolites du Queyras (Alpes franco-italiennes): données  
570 nouvelles et précisions lithostratigraphiques. C. R. Acad. Sc. Paris, II, 292:1405-1408.

571 Lagabrielle Y., Polino R., Auzende J.M., Blanchet R., Caby R., Fudral S., Lemoine M., Mevel C.,  
572 Ohnestetter M., Robert D. and Tricart P., 1984. Les témoins d'une tectonique intraocéanique  
573 dans le domaine téthysien: analyse du rapport entre les ophiolites et leur couvertures  
574 métasédimentaires dans la zone piémontaise des Alpes franco-italiennes. *Ofioliti*, 9: 67-88

575 Lemoine M., 1971. Données nouvelles sur la Série du Gondrand près de Briançon (Alpes  
576 Cottiennes). Réflexion sur les problèmes stratigraphiques et paléogéographiques de la zone  
577 piémontaise. *Géol. Alpine*, 47: 181-201.

578 Lemoine M., Bas T., Arnaud-Vanneau A., Arnaud A., Dumont T., Gidon M., Bourbon M., de  
579 Graciansky P. C., Rudkiewicz J. L., Mégard-Galli J. and Tricart P., 1986. The continental  
580 margin of the Mesozoic Tethys in the Western Alps. *Mar. Petrol. Geol.*, 3, 179-199.

581 Lemoine M. and Tricart P., 1986. Les Schistes lustrés piémontais des Alpes Occidentales: approche  
582 stratigraphique, structurale et sédimentologique. *Eclogae geol. Helv.*, 79: 271-294

583 Lemoine, M. and Trümpy, R., 1987. Pre-oceanic rifting in the Alps. *Tectonophysics*, 133(3-4): 305-  
584 320.

585 Malusà M. G., Mosca P., Borghi A., Dela Pierre F. and Polino R., 2002. Approccio multi-  
586 disciplinare per la ricostruzione dell'assetto tettono-stratigrafico e dell'evoluzione metamorfico-  
587 strutturale di un settore di catena orogenica: l'esempio dell'Alta Valle di Susa (Alpi occidentali).  
588 *Mem. Soc. Geol. It.*, 57: 249-257.

589 Manatschal G., 2004. New models for evolution of magma-poor rifted margins based on a review of  
590 data and concepts from West Iberia and the Alps. *Int. J. Earth Sci.*, 93: 432-466.

591 Manatschal G. and Müntener O., 2009. A type sequence across an ancient magma-poor ocean-  
592 continent transition: the example of the western Alpine Tethys ophiolites. *Tectonophysics*, 473:  
593 4-19.

- 594 Martin S., Tartarotti P. and Dal Piaz G. V., 1994. The Mesozoic ophiolites of the Alps: a review.  
595 Boll. Geof. Teor. Appl.,36, (141-144): 175-216.
- 596 Maruyama S., Moonup C. and Liou J.C., 1986. Experimental investigations of blueschist-  
597 greenschist transition equilibria: pressure dependence of Al<sub>2</sub>O<sub>3</sub> contents in sodic amphiboles –  
598 a new geobarometer. Geol. Soc. Am. Mem., 146: 1-16.
- 599 Massonne H.J. and Schreyer W., 1987. Phengite geobarometry based on the limiting assemblage  
600 with K-feldspar, phlogopite and quartz. Contr. Miner. Petrol., 96: 212-224.
- 601 Mevel, C., Caby, R. and Kienast, J.R., 1978. Amphibolite facies conditions in the oceanic crust:  
602 example of amphibolitized flaser gabbro and amphibolites from the Chenaillet ophiolite massif  
603 (Hautes Alpes, France). Earth Planet. Sci. Lett. 39: 98–108.
- 604 Mohn G., Manatschal G., Beltrando M., Masini E. and Kuszniir N., 2012. Necking of continental  
605 crust in magma-poor rifted margins: Evidence from the fossil Alpine Tethys margins. Tectonics,  
606 31, TC1012, doi:10.1029/2011TC002961.
- 607 Molli G., Crispini L., Malusà M. G., Mosca P., Piana F. and Federico L., 2010. Geology of the  
608 Western Alps-Northern Apennine junction area: a regional review. J. Virtual Explorer, 36, paper  
609 10, Doi: 10.3809/jvirtex.2010.00215
- 610 Morimoto N., 1988. Nomenclature of pyroxenes. Schweiz. Mineral. Petrogr. Mitt.,68: 95-111.
- 611 Palin R.M. and White R.W., 2016. Emergence of blueschists on Earth linked to secular changes in  
612 oceanic crust composition. Nature Geosciences, 9, 60-65.
- 613 Petrakakis K. and Dietrich H., 1985. MINSORT: A program for the processing and archivation of  
614 microprobe analysis of silicate and oxide minerals. N. Jb. Miner. Mh.,8: 379-384.
- 615 Poli S. and Schmidt M.W., 1995. H<sub>2</sub>O transport and release in subduction zones: Experimental  
616 constraints on basaltic and andesitic systems. J. Geoph. Res., 100: 22299-22314.
- 617 Polino R., 1984. Les séries océaniques du haut Val de Suse (Alpes Cottiennes): analyse des  
618 couvertures sédimentaires. Ofioliti, 9: 547-554.

619 Polino R. and Lemoine M., 1984. Détritisme mixte d'origine continentale et océanique dans les  
620 sédiments jurassico-crétacés supra-ophiolitiques de la Téthys ligure: la série du Lago Nero  
621 (Alpes Occidentales franco-italiennes). C.R. Acad. Sci., Série 2, 298(8): 359-364.

622 Proyer A., 2003. Metamorphism of pelites in NKFMAH—a new petrogenetic grid with  
623 implications for the preservation of high-pressure mineral assemblages during exhumation.  
624 Journal of metamorphic Geology, 21(5): 493-509.

625 Roure F., Heitzmann P. and Polino R., 1990. Deep structure of the Alps. Mém. Soc. géol. Fr., 156;  
626 Mém. Soc. géol. suisse, 1; Vol. spec. Soc. Geol. It., 1, pp. 367.

627 Servizio Geologico d'Italia, 1911. Carta Geologica d'Italia alla scala 1:100.0000, F. 66 Cesana T.se.  
628 Roma.

629 Servizio Geologico di Italia, 2002. Carta Geologica d'Italia alla scala 1:50.0000, F. 132-152-153  
630 Bardonecchia with explanatory notes by Polino R. (coord.) et alii., ISPRA, Roma.  
631 [http://www.isprambiente.gov.it/Media/carg/153\\_BARDONECCHIA/Foglio.html](http://www.isprambiente.gov.it/Media/carg/153_BARDONECCHIA/Foglio.html)

632 Servizio Geologico di Italia, in press. Carta Geologica d'Italia alla scala 1:50.0000, F. 171 Cesana  
633 by Polino R. (coord.), Fioraso G., Malusà M. and Mosca P., ISPRA, Roma.  
634 [http://www.isprambiente.gov.it/Media/carg/171\\_CESANA\\_TORINESE/Foglio.html](http://www.isprambiente.gov.it/Media/carg/171_CESANA_TORINESE/Foglio.html)

635 Spear F. S. and Cheney, J. T., 1989. A petrogenetic grid for pelitic schists in the system SiO<sub>2</sub>-Al<sub>2</sub>O<sub>3</sub>-FeO-MgO-K<sub>2</sub>O. Contr. Min. and Petr., 101(2): 149-164.

637 Tartarotti P., Festa A., Benciolini L. and Balestro G. 2017. Record of Jurassic mass transport  
638 processes through the orogenic cycle: Understanding chaotic rock units in the high-pressure  
639 Zermatt-Saas ophiolite (Western Alps). Lithosphere, 9(3): 399-407.

640 Tricart P., 1984. From passive margin to continental collision; a tectonic scenario for the Western  
641 Alps. Am. Journ. Sci. 284(2): 97-120.

642

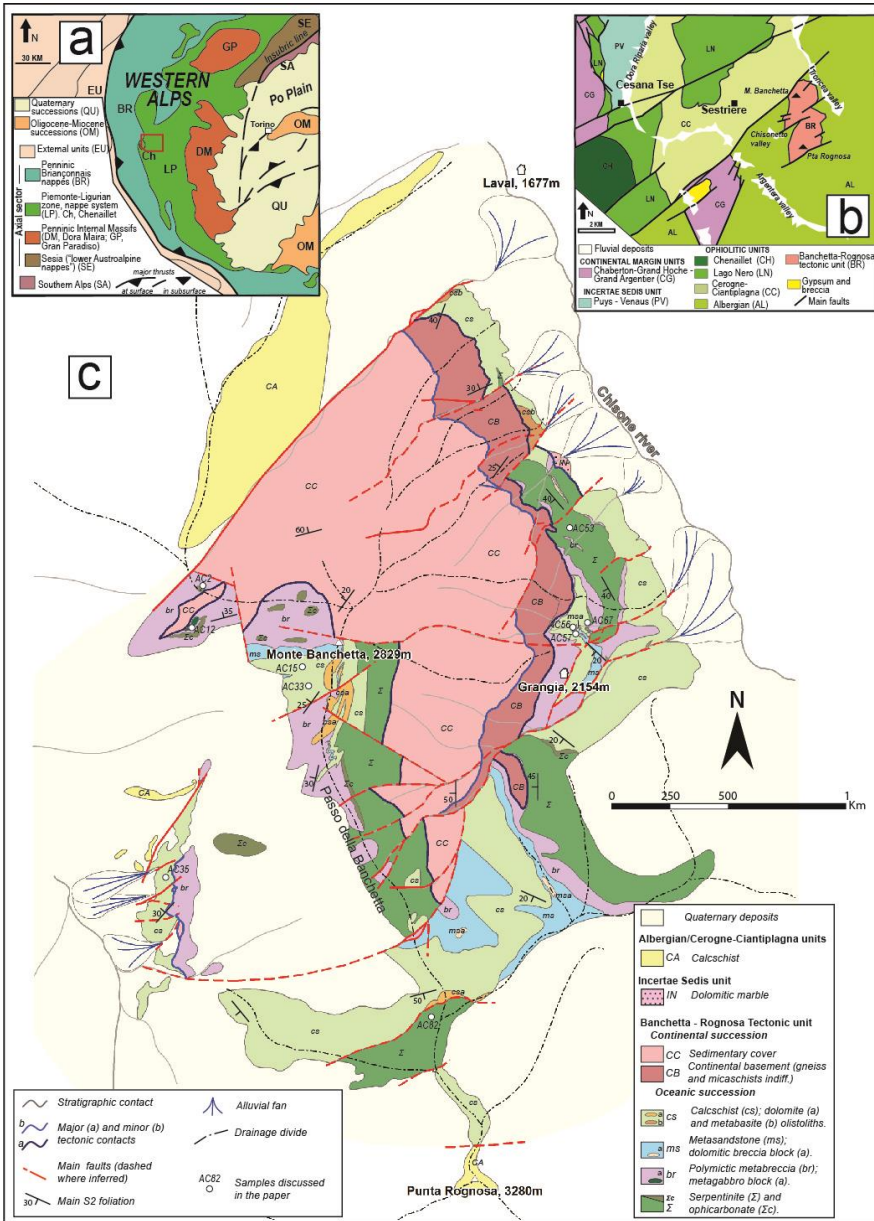


Fig 1 Corno et al.  
(180 mm, full page)

643

644

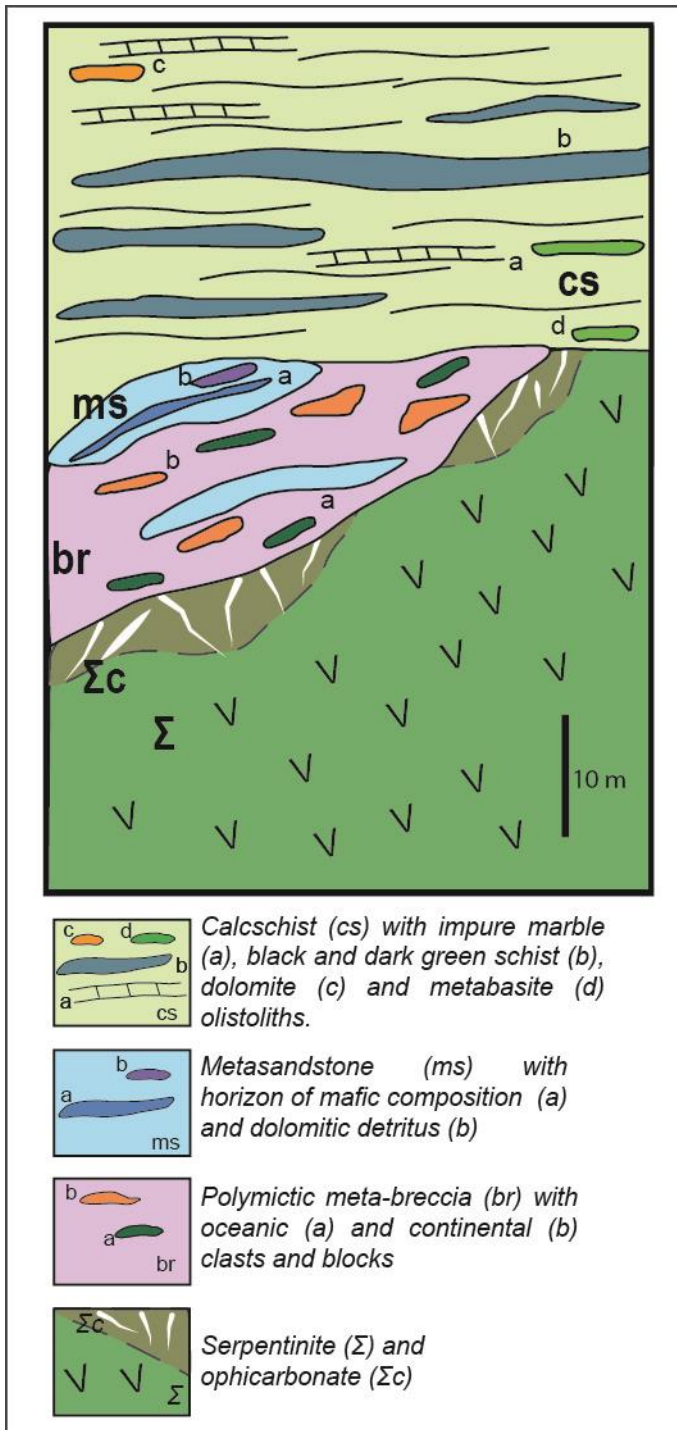


Fig 2. Corno et al  
(85 mm)

645

646

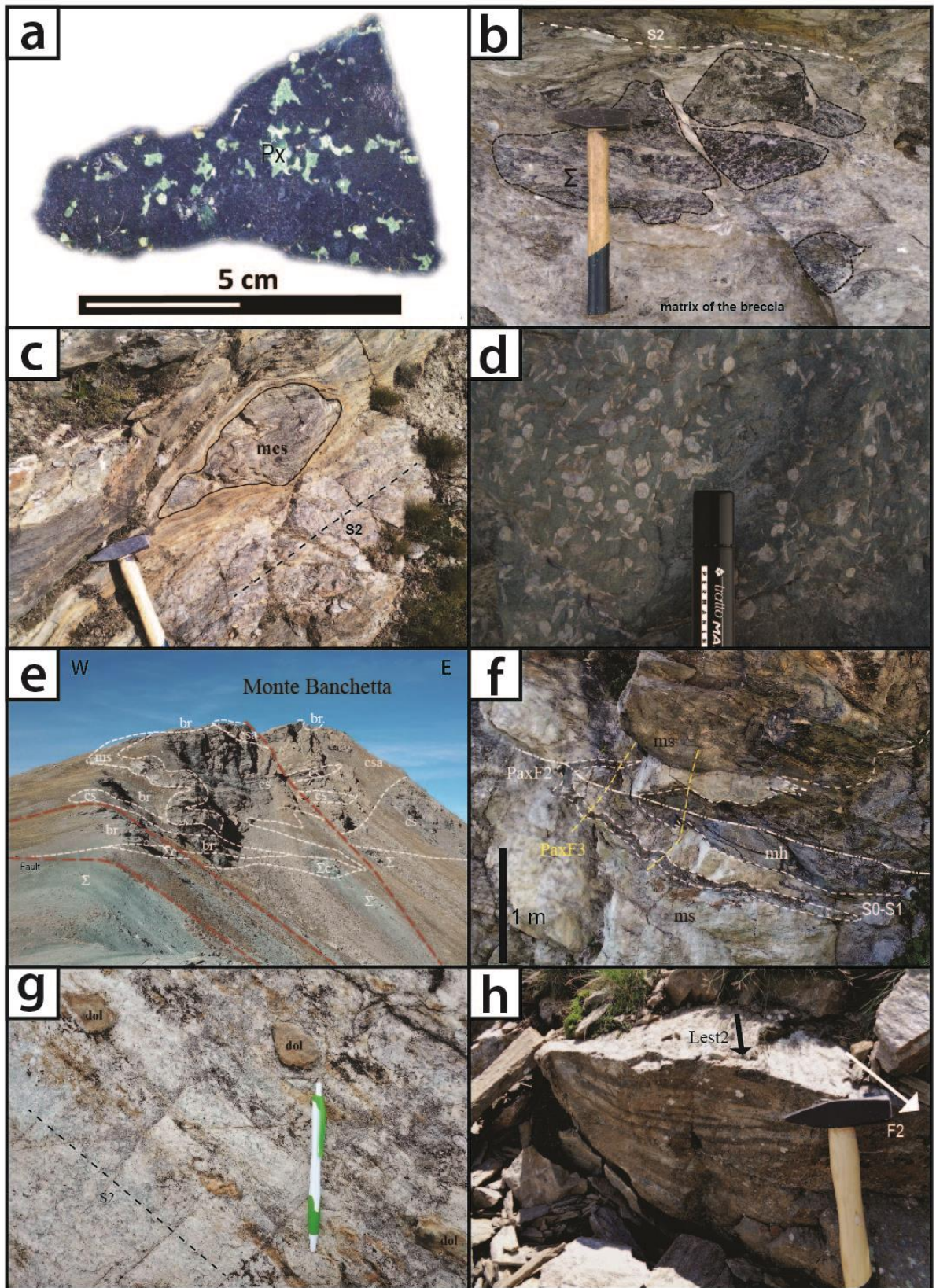


Fig. 3 Corno et al.  
(full page)

647

648

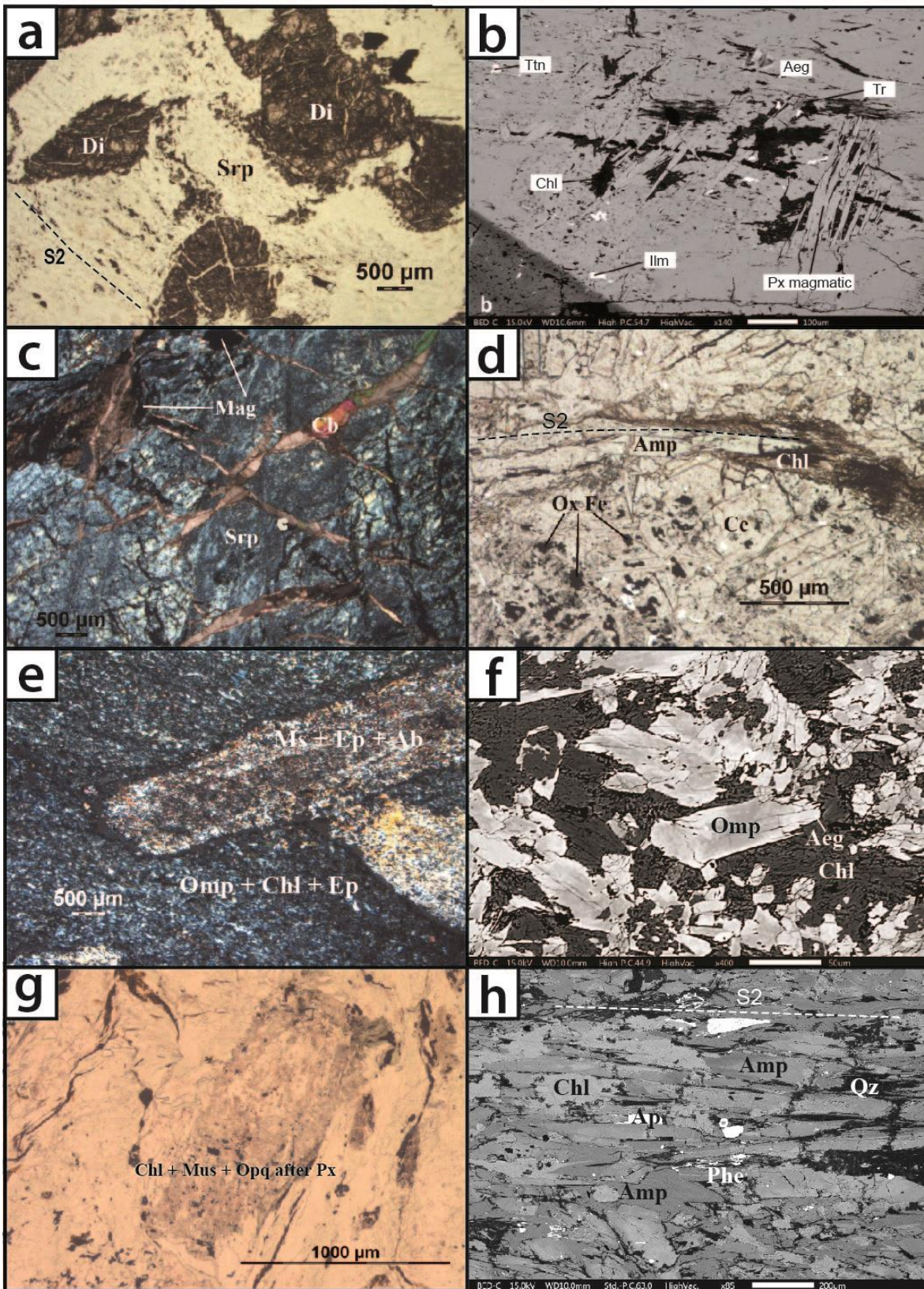


Fig. 4 Corno et al.  
(180 mm)

649

650

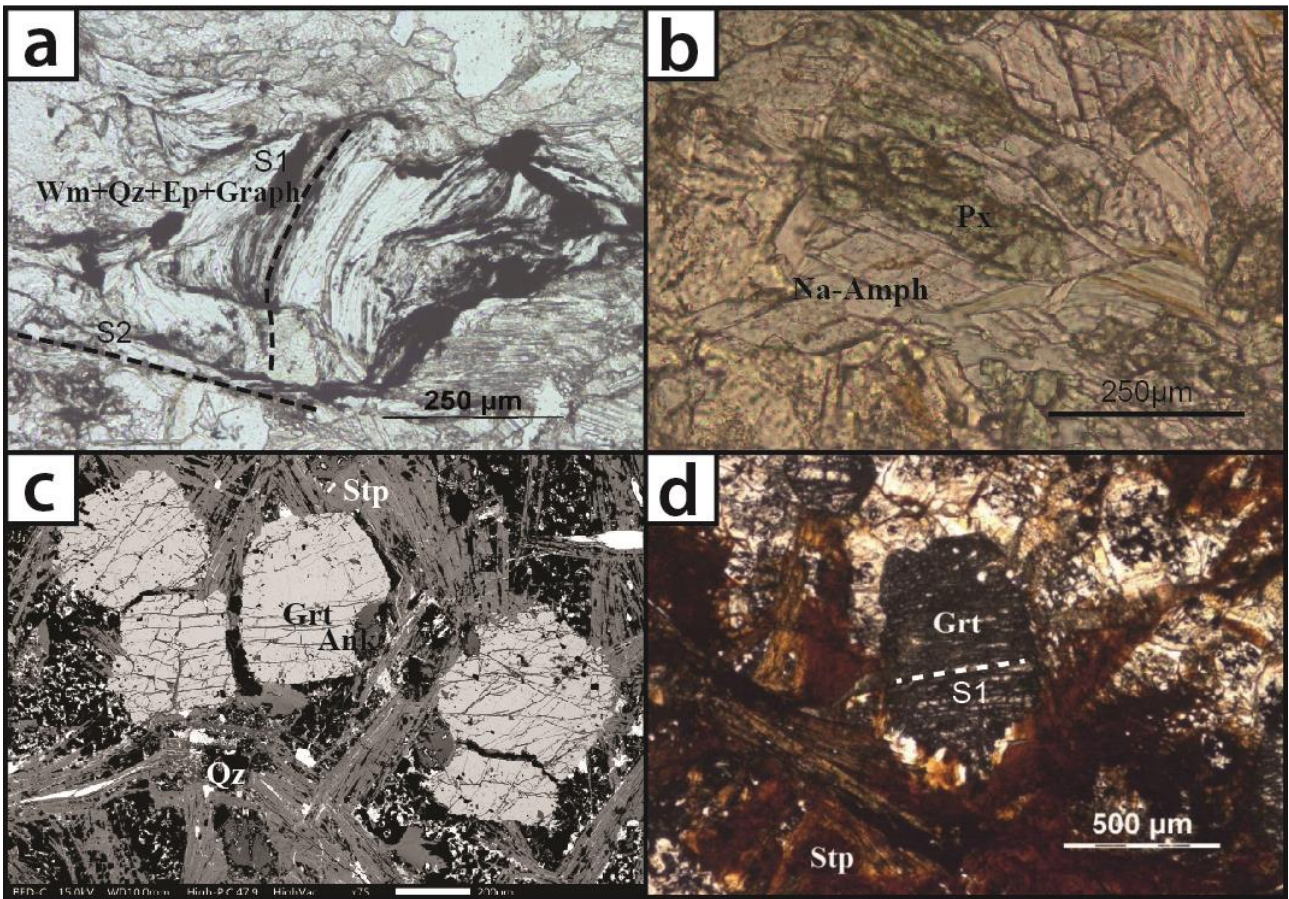


Fig. 5 Corno et al.  
(180 mm)

651

652

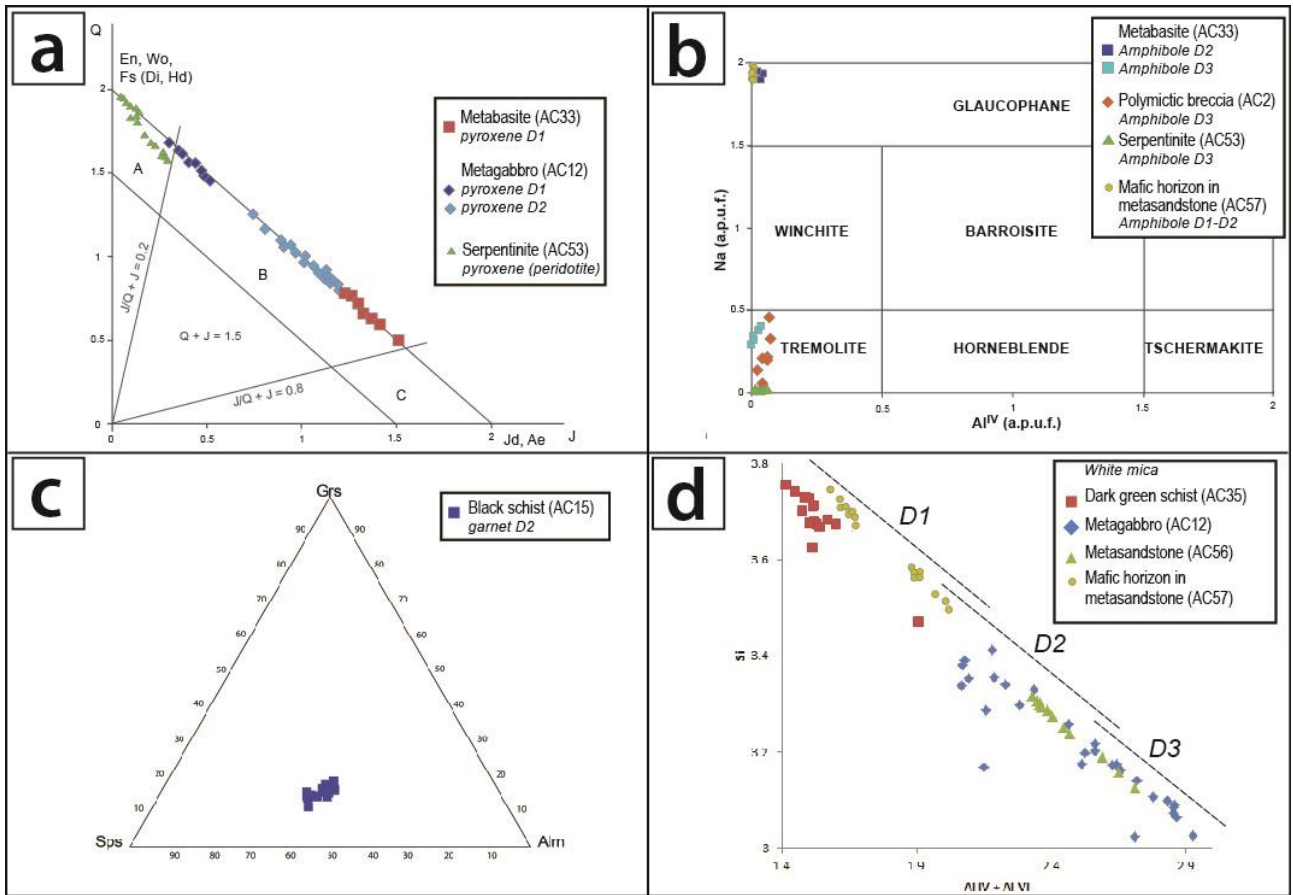


Fig. 6 Corno et al.  
(180 mm)

653

654

655

		Pre-D1	D1	D2	D3+D4
<b>Ultrabasic rocks</b>	Pyroxene	Di	Aeg-aug	Aeg-aug	
	Serpentine				
	Amphibole				
	Chlorite				
	Magnetite		-----		
<b>Ophicarbonate</b>	Carbonate				
	Amphibole			Act	Tr
	Chlorite				
<b>Meta-gabbro</b>	Pyroxene	Di?	Ump	Aeg-aug	
	Chlorite				
	Plagioclase				Ab
	Epidote				
	White mica			Phe	Ms
	Pumpellyite				
	Titanite				
<b>Metabasite</b>	Quartz				
	Amphibole			Gln	Tr
	Pyroxene		Aeg-aug		
	White mica			Phe	Ms
	Chlorite				
	Epidote		-----		
	Albite				
	Carbonate				
	Pumpellyite				
Rutile					
<b>Metasandstone</b>	Quartz				
	White mica		-----	Phe	Ms
	Chlorite				
	Chloritoid				
	Stilpnomelane				
	Carbonate				
	Rutile				
	Amphibole		Gln	Gln	
<b>Calcschist</b>	Carbonate				
	Quartz				
	Chlorite				
	White mica				
	Graphite				
	Lawsonite		---		
	Epidote		-----		
<b>Black and green schists</b>	Quartz				
	White mica				
	Chlorite				
	Stilpnomelane				
	Garnet		-----		
	Amphibole		-----		
	Carbonate		-----		
	Ankerite		-----		

Fig. 7 Corno et al.

656

657

658

659

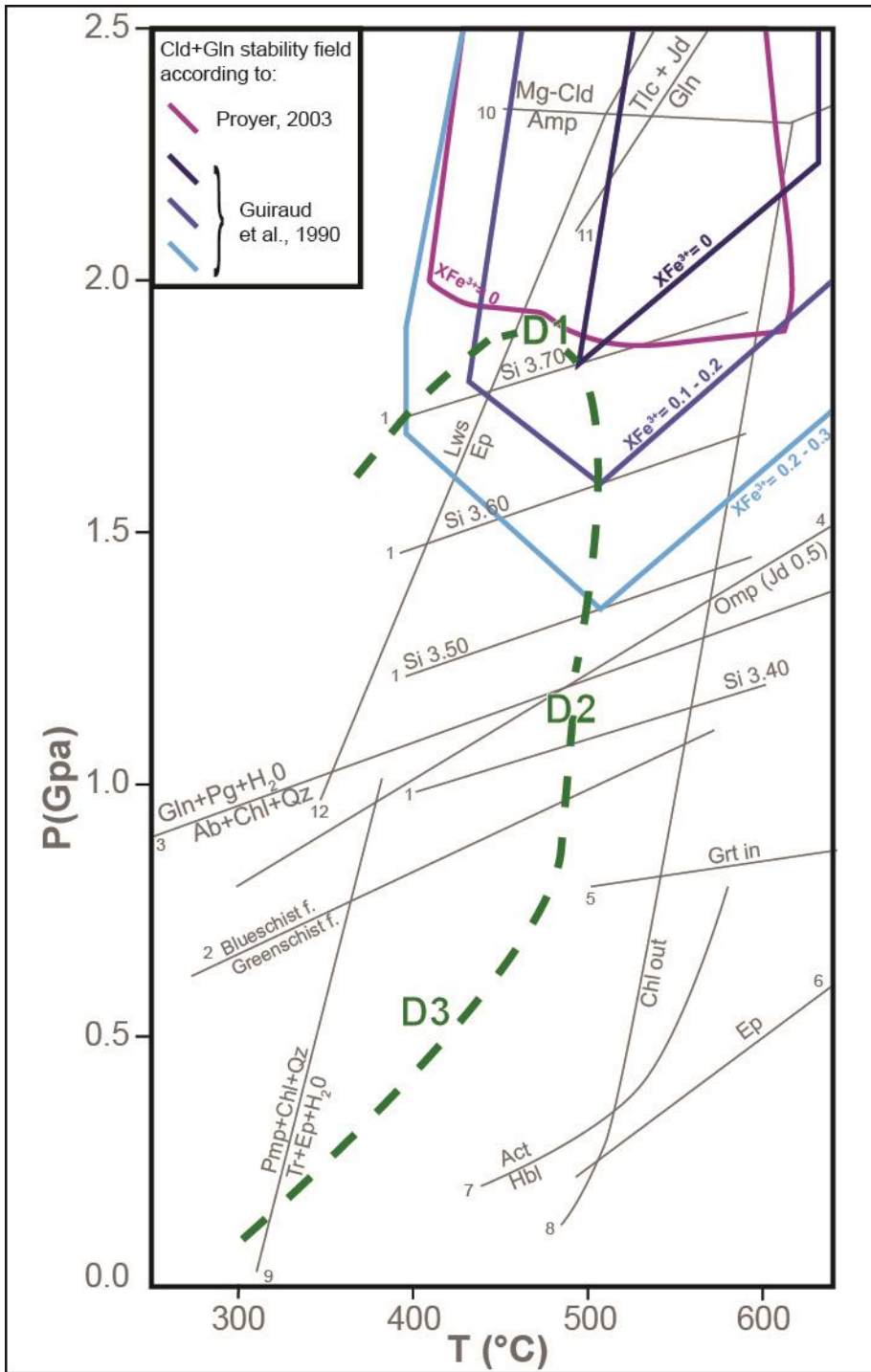


Fig 8. Como et al  
(120 mm)

660

661

662

663

664

Table 1. Representative SEM-EDX analyses of clinopyroxene (omph = omphacite; aeg-au = aegirine – augite; diop = diopside) calculated on the basis of 6 oxygens and 4 cations. bdl: below detection limit.

Sample Analysis	AC12 35	AC12 34	AC12 12	AC12 37	AC12 40	AC12 41	AC33 52	AC33 54	AC33 59	AC53 63	AC53 67	AC53 72
mineral	omph	omph	omph	aeg-au	aeg-au	aeg-au	aeg-au	aeg-au	aeg-au	diop	diop	diop
SiO2	55.76	56.61	55.86	54.87	54.33	54.54	53.72	54.05	54.66	55.87	55.40	54.58
TiO2	bdl											
Al2O3	6.99	8.65	7.84	2.37	1.17	2.84	1.62	0.81	2.28	0.00	0.00	0.00
Cr2O3	0.40	0.31	bdl	0.44	0.44	0.34	0.76	0.61	1.54	0.43	0.47	0.69
FeO	8.12	7.73	7.06	11.40	7.40	11.34	11.89	11.10	9.63	2.66	2.85	2.72
MnO	bdl	bdl	0.41	0.35	0.45	0.37	bdl	0.39	0.48	bdl	bdl	bdl
MgO	8.55	7.87	8.53	10.22	13.28	9.68	9.80	11.09	10.21	17.94	18.18	17.52
CaO	12.41	10.81	12.23	15.60	19.98	14.55	17.98	18.54	15.79	24.16	23.58	23.97
Na2O	7.60	8.52	7.71	5.65	2.87	6.06	4.72	3.46	5.31	0.44	0.40	0.45
	*****	*****	*****	*****	*****	*****	*****	*****	*****	*****	*****	*****
Total	99.83	100.50	99.65	100.89	99.91	99.73	100.49	100.04	99.88	101.49	100.89	99.94
Si	1.994	1.998	1.993	1.982	1.986	1.988	1.968	1.998	1.998	1.997	1.991	1.983
Al IV	0.006	0.002	0.007	0.018	0.014	0.012	0.032	0.002	0.002	0.000	0.000	0.000
Fe 3+	0.000	0.000	0.000	0.000	0.000	0.000	0.000	0.000	0.000	0.002	0.007	0.012
Cr IV	0.000	0.000	0.000	0.000	0.000	0.000	0.000	0.000	0.000	0.001	0.003	0.005
Al VI	0.288	0.358	0.323	0.083	0.037	0.110	0.038	0.033	0.096	0.000	0.000	0.000
Ti	0.000	0.000	0.000	0.000	0.000	0.000	0.000	0.000	0.000	0.000	0.000	0.000
Cr VI	0.011	0.008	0.000	0.012	0.013	0.01	0.022	0.018	0.044	0.011	0.011	0.015
Fe 3+	0.234	0.219	0.217	0.319	0.167	0.321	0.308	0.199	0.238	0.023	0.027	0.034
Fe 2+	0.008	0.009	-0.006	0.025	0.058	0.025	0.056	0.141	0.055	0.052	0.049	0.035
Mn	0.000	0.000	0.013	0.011	0.014	0.012	0.000	0.012	0.015	0.000	0.000	0.000
Mg	0.456	0.406	0.454	0.55	0.711	0.523	0.535	0.597	0.552	0.914	0.913	0.916
Fe 2+	0.000	0.000	0.000	0.000	0.001	0.000	0.000	0.003	0.001	0.002	0.003	0.001
Mn	0.000	0.000	0.000	0.000	0.000	0.000	0.000	0.000	0.000	0.000	0.000	0.000
Mg	0.000	0.008	0.000	0.000	0.013	0.003	0.000	0.014	0.005	0.042	0.061	0.034
Ca	0.475	0.409	0.467	0.604	0.783	0.568	0.705	0.734	0.618	0.925	0.908	0.933
Na	0.527	0.583	0.533	0.396	0.203	0.429	0.335	0.248	0.376	0.030	0.028	0.032
T	2.000	2.000	2.000	2.000	2.000	2.000	2.000	2.000	2.000	2.000	2.000	2.000
M(1)	0.998	1.000	1.000	1.000	1.000	1.000	0.959	1.000	1.000	1.000	1.000	1.000
M(2)	1.002	1.000	1.000	1.000	1.000	1.000	1.041	1.000	1.000	1.000	1.000	1.000

665

666

Table 2. Representative SEM-EDX analyses of garnet calculated on the basis of 12 oxygens and 8 cations. bld: below detection limit. End member abbreviations: alm = almandine; sp = spessartine; px = pyrope; grs = grossular; an = andradite

Sample	AC15	AC15	AC15	AC15	AC15							
Analysis	1	4	5	6	7	8	9	10	11	12	13	14
mineral	grt	grt	grt	grt	grt							
SiO2	36.49	36.53	36.54	36.58	36.68	36.34	36.38	36.17	36.70	36.75	37.30	37.08
TiO2	<u>bld</u>	0.36	<u>bld</u>	<u>bld</u>	0.39							
Al2O3	20.53	20.65	20.58	20.46	20.45	20.52	20.45	20.37	20.50	20.68	20.79	20.48
FeO	18.25	18.48	18.43	18.67	17.64	15.82	18.14	15.95	16.32	17.93	18.51	17.07
MnO	17.77	18.65	17.82	17.14	17.97	20.58	16.99	20.66	20.32	17.84	17.77	21.17
MgO	0.00	0.00	0.29	0.31	0.00	0.00	0.00	0.00	0.00	0.29	0.00	0.00
CaO	5.97	5.21	6.01	5.94	6.45	5.37	6.51	5.10	5.45	6.39	6.34	4.70
	*****	*****	*****	*****	*****	*****	*****	*****	*****	*****	*****	*****
Total	99.01	99.52	99.66	99.11	99.20	98.63	98.46	98.25	99.66	99.88	100.71	100.89
Si	2.998	2.992	2.980	2.997	3.003	2.999	3.000	3.000	2.998	2.986	3.008	3.000
Al IV	0.002	0.008	0.020	0.003	0.000	0.001	0.000	0.000	0.002	0.014	0.000	0.000
Al VI	1.985	1.986	1.959	1.973	1.974	1.995	1.987	1.990	1.972	1.967	1.976	1.952
Ti	0.000	0.000	0.000	0.000	0.000	0.000	0.000	0.000	0.022	0.000	0.000	0.024
Fe 3+	0.015	0.015	0.046	0.028	0.025	0.005	0.013	0.010	0.002	0.037	0.022	0.021
Fe 2+	1.238	1.250	1.211	1.251	1.183	1.086	1.239	1.096	1.113	1.182	1.226	1.134
Mn	1.237	1.294	1.231	1.189	1.246	1.438	1.186	1.451	1.406	1.228	1.214	1.451
Mg	0.000	0.000	0.035	0.038	0.000	0.000	0.000	0.000	0.000	0.035	0.000	0.000
Ca	0.525	0.457	0.525	0.522	0.566	0.475	0.575	0.453	0.477	0.556	0.547	0.407
Z	3.000	3.000	3.000	3.000	3.003	3.000	3.000	3.000	3.000	3.000	3.008	3.000
Y	2.001	2.002	2.005	2.001	1.999	2.000	2.000	2.000	1.996	2.003	1.998	1.997
X	3.000	3.001	3.003	3.000	2.995	3.000	3.000	3.000	2.996	3.002	2.987	2.992
<u>alm</u>	0.413	0.417	0.403	0.417	0.395	0.362	0.413	0.365	0.372	0.394	0.410	0.379
<u>sp</u>	0.412	0.431	0.410	0.396	0.416	0.479	0.396	0.484	0.469	0.409	0.406	0.485
<u>px</u>	0.000	0.000	0.012	0.013	0.000	0.000	0.000	0.000	0.012	0.012	0.000	0.000
<u>grs</u>	0.168	0.145	0.152	0.160	0.176	0.156	0.185	0.146	0.147	0.167	0.172	0.114
<u>an</u>	0.008	0.008	0.023	0.014	0.013	0.003	0.006	0.005	0.012	0.018	0.011	0.023

667

668

Table 3. Representative SEM-EDX analyses of dioctahedral calculated on the basis of 11 oxygens and 7 cations. bdl: below detection limit

Sample	AC12	AC12	AC12	AC35	AC35	AC35	AC56	AC56	AC56	AC57	AC57	AC57
Analysis	10.00	4.00	6.00	29.00	39.00	40.00	47.00	48.00	50.00	59.00	60.00	61.00
<u>mineral</u>	<u>mica</u>											
SiO2	50.31	46.90	45.43	54.17	53.60	53.42	48.36	47.40	47.16	55.61	52.32	54.43
Al2O3	27.27	31.52	37.30	17.33	18.13	18.74	29.28	30.27	32.48	19.95	24.72	20.99
Cr2O3	<u>bdl</u>	<u>bdl</u>	0.00	1.58	2.65	2.51	<u>bdl</u>	<u>bdl</u>	<u>bdl</u>	<u>bdl</u>	<u>bdl</u>	<u>bdl</u>
FeO	1.55	2.79	1.21	5.11	4.70	4.67	3.99	3.83	3.37	2.04	2.01	1.98
MgO	3.55	2.56	0.44	4.74	4.35	4.25	1.76	1.43	0.87	5.63	4.26	5.41
CaO	<u>bdl</u>											
Na2O	<u>bdl</u>	0.31	0.55	<u>bdl</u>	<u>bdl</u>	<u>bdl</u>	0.28	0.35	0.55	<u>bdl</u>	<u>bdl</u>	<u>bdl</u>
K2O	10.58	10.19	9.66	10.22	10.23	10.17	10.35	10.04	9.77	10.71	10.59	10.53
	*****	*****	*****	*****	*****	*****	*****	*****	*****	*****	*****	*****
Total	93.27	94.27	94.59	93.15	93.65	93.78	94.02	93.32	94.19	93.94	93.91	93.35
Si	6.825	6.351	6.051	7.509	7.402	7.360	6.595	6.501	6.380	7.487	7.056	7.373
Al IV	1.175	1.649	1.949	0.491	0.598	0.640	1.405	1.499	1.620	0.513	0.944	0.627
Al VI	3.185	3.381	3.907	2.341	2.352	2.403	3.302	3.396	3.559	2.652	2.985	2.724
Cr	0.000	0.000	0.000	0.173	0.289	0.274	0.000	0.000	0.000	0.000	0.000	0.000
Fe	0.176	0.316	0.134	0.592	0.543	0.538	0.455	0.439	0.382	0.230	0.227	0.225
Mg	0.718	0.516	0.089	0.980	0.894	0.873	0.358	0.292	0.175	1.128	0.856	1.093
Ca	0.000	0.000	0.000	0.000	0.000	0.000	0.000	0.000	0.000	0.000	0.000	0.000
Na	0.000	0.080	0.141	0.000	0.000	0.000	0.075	0.093	0.142	0.000	0.000	0.000
K	1.832	1.760	1.641	1.807	1.801	1.789	1.801	1.757	1.686	1.839	1.823	1.820
Z	8.000	8.000	8.000	8.000	8.000	8.000	8.000	8.000	8.000	8.000	8.000	8.000
Y	4.079	4.214	4.130	4.085	4.078	4.087	4.114	4.127	4.116	4.011	4.068	4.042
X	1.832	1.840	1.783	1.807	1.801	1.789	1.875	1.849	1.829	1.839	1.823	1.820

669

670

Table 4. Representative SEM-EDX analyses of amphibole (trem=tremolite, gln=glaucoophane) calculated on the basis of 23 oxygens. bdl=below detection limit.

Sample	AC2	AC2	AC2	AC2	AC 44	AC 44	AC 44	AC 44
Analysis	8.00	4.00	7.00	9.00	14	15	16	12
mineral	trem	trem	trem	trem	gln	gln	gln	gln
SiO2	58.32	58.43	58.04	58.17	57.61	57.78	57.11	58.84
Al2O3	bdl	bdl	bdl	bdl	8.32	7.19	6.35	12.00
Cr2O3	bdl	0.38	0.41	0.43	bdl	bdl	bdl	bdl
FeO	3.77	4.35	3.38	4.11	15.45	17.09	17.64	9.39
MgO	22.31	22.14	22.59	22.05	9.18	9.12	9.20	9.91
CaO	12.98	12.34	13.27	12.58	0.58	0.40	0.37	bdl
Na2O	0.48	0.89	0.28	0.70	7.17	7.38	7.36	7.88
	*****	*****	*****	*****	*****	*****	*****	*****
Total	97.86	98.54	97.97	98.04	98.31	98.96	98.03	98.02
Si	8.004	7.965	7.953	7.975	7.964	7.979	7.977	8.000
Al IV	-0.004	0.035	0.047	0.025	0.036	0.021	0.023	0.000
Al VI	0.004	-0.035	-0.047	-0.025	1.321	1.149	1.024	1.924
Cr	0.000	0.041	0.045	0.047	0.000	0.000	0.000	0.000
Fe 3+	0.045	0.189	0.076	0.122	0.627	0.771	0.898	0.000
Mg	4.564	4.499	4.616	4.507	1.894	1.878	1.916	2.009
Fe 2+	0.387	0.306	0.310	0.350	1.159	1.201	1.162	1.068
Fe 2+	0.000	0.000	0.000	0.000	0.000	0.000	0.000	0.001
Ca	1.909	1.802	1.949	1.847	0.086	0.060	0.055	0.000
Na	0.091	0.198	0.051	0.153	1.914	1.940	1.945	1.999
Na	0.037	0.038	0.024	0.034	0.002	0.040	0.046	0.075
K	0.000	0.000	0.000	0.000	0.000	0.000	0.000	0.000

671

672

Table 5. Representative SEM-EDX analyses of chloritoid (cld) calculated on the basis of 12 oxygens. bdl: below detection limit.

Sample	AC15	AC15	AC15	AC15
Analysis	11	12	13	14
mineral	cld	cld	cld	cld
SiO <sub>2</sub>	24.87	25.36	25.32	25.04
Al <sub>2</sub> O <sub>3</sub>	41.57	41.25	41.59	41.21
FeO	22.64	22.57	22.26	22.14
MnO	1.86	1.98	1.57	1.97
MgO	2.66	2.53	2.72	2.55
CaO	0.00	0.00	0.00	0.00
	*****	*****	*****	*****
Total	93.60	93.69	93.47	92.90
Si	2.021	2.056	2.051	2.046
Al	3.002	2.999	3.021	3.014
Fe	1.538	1.531	1.508	1.512
Mn	0.128	0.136	0.108	0.136
Mg	0.322	0.307	0.329	0.310
Ca	0.000	0.000	0.000	0.000

673

674